metals

Article

Local Strengthening Design and Compressive Behavior Study of the Triangular Honeycomb Structure

Qian Zhang [1], Wenwang Wu [2] and Jianlin Liu [1,*]

[1] College of Pipeline and Civil Engineering, China University of Petroleum (East China), Qingdao 266580, China
[2] School of Naval Architecture, Ocean & Civil Engineering, Shanghai Jiao Tong University, Shanghai 200240, China
* Correspondence: liujianlin@upc.edu.cn; Tel./Fax: +86-0532-86981822

Abstract: Additive manufacturing (AM) enables diversity in honeycomb structure configuration, which benefits optimization of the honeycomb structure. In the present study, we proposed two locally enhanced triangular honeycomb structures to improve in-plane compressive performance by avoiding diagonal fracture band. The compressive behaviors and failure mechanism of the original and enhanced triangular honeycomb structures made of 316L steel were studied by experiments and numerical simulations. The results show that the cell-enhanced triangular honeycomb structure and wall-enhanced triangular honeycomb structure possess significantly improved stiffness and peak load compared with the original structure. The fracture band along the diagonal direction of the triangular honeycomb structure is caused by buckling of the cell wall, which is related to its topologic structure. Stress distribution is an essential index reflecting the performance of a honeycomb structure. Uniform stress distribution makes the honeycomb structure fail layer by layer, and it can improve the peak load of the honeycomb structure. Defects such as unmelted metal particles and voids caused by AM processing weaken the strength and plasticity, and the resulting brittleness makes the honeycomb structure fall into pieces.

Keywords: additive manufacturing; triangular honeycomb structure; enhancing; in-plane compression; microstructure

Citation: Zhang, Q.; Wu, W.; Liu, J. Local Strengthening Design and Compressive Behavior Study of the Triangular Honeycomb Structure. *Metals* **2022**, *12*, 1779. https://doi.org/10.3390/met12111779

Academic Editor: Antonio Mateo

Received: 16 September 2022
Accepted: 20 October 2022
Published: 22 October 2022

1. Introduction

Honeycomb structures are widely used in aerospace, high-speed railway and vehicle engineering because their light weight and multifunctionality can meet the requirements of weight reduction and compactness [1–3]. In recent years, development of additive manufacturing (AM) has promoted structural improvement in the honeycomb structure [4–7], which is not limited to a structure with a unified unit cell of traditional hexagonal [8–10], square [11], circular [12], kagome [13] and triangular [14] shape, etc. To enhance the in-plane strength of the circular honeycomb, Liu et al. [15] proposed a novel structure composed of semi-periodic sinusoidal beams. The deformation behaviors were studied by the theoretical method and finite element analysis. Similar design ideas were also used to improve the crashworthiness and energy absorption performance of honeycomb structures, and the quadri-arc [16] and petal-shaped [17] elements were applied. Peng et al. [18] proposed a kind of honeycomb structure with a unit cell of two merged hexagons; the stiffness was enhanced, and the effective elastic thermoelastic properties of the honeycomb structure can be widely tunable by adjusting the microstructural geometry and constituent materials.

Hierarchical structures in nature have inspired people's ideas regarding hierarchical design of the honeycomb structure [19–22]. The formal cell wall of a honeycomb structure can be replayed by the topology structure composed of a hexagon, triangle, etc., and the compressive strength and energy absorption of the hierarchical honeycomb structures are improved obviously [23–26]. Li et al. [27] designed a hierarchical triangular honeycomb structure with T-ribs to improve buckling resistance and plastic performance. Fan et al. [28] proposed a hierarchical rectangle tubular structure with three folding modes, including macro-cell folding, micro-cell folding and hybrid folding under crushing, and excellent energy absorption performance was achieved. Using smaller geometric cells instead of cell nodes in a honeycomb structure is also a design method of hierarchical structure. The hexagonal hierarchical honeycombs from first to fourth order were designed by Oftodeh et al. [29]; they found that the in-plane stiffness and strength were, respectively, two to eight times and two times higher than a regular honeycomb with the same density. Similar structures were also found to have better energy absorption and dynamic failure properties [30,31].

For metal AM honeycomb structures, the stiffness and strength properties are not only related to cell topology but also affected by the geometric defects and microstructure of metal [32]. Plessis et al. [33] performed a quasi-static compression test on the Ti6Al4V gyroid structures made by laser power bed fusion to analyze the effects of microporosity. It was found that a lack of fusion seriously endangers the compression performance, and there are cracks along the diagonals of the failed gyroid lattice samples, which results in ultimate failure. Poach et al. [34] pointed out that the surface roughness caused by the AM process influences the strength of the structure. The triangular honeycomb structure is one of the strongest, stiffest and toughest two-dimensional lattices [35]. However, it was found by experiment that the triangular honeycomb structure is easily destructed along the diagonal direction (fracture band) under in-plane compression [27]. In this paper, to improve the in-plane compression capacity, locally hierarchically enhanced triangular honeycomb structures were proposed, and the compression mechanical behaviors of the original and locally enhanced triangular honeycomb structures made of 316L steel by using selective laser melting (SLM) were studied. Both experiments and numerical simulations were performed to verify the efficiency of the locally enhanced structure and clarify the mechanism of the failure modes. The effects of manufacturing defects and the metallographic structure on the compressive behaviors of the triangular honeycomb structures were analyzed in detail.

2. Experiment

In order to avoid global failure due to local fracture bands under in-plane compression, cell-enhanced and wall-enhanced triangular honeycombs are designed at the first step. The schematic drawings of the triangular honeycomb structures are shown in Figure 1. For the 4×4 original triangular honeycomb, as shown in Figure 1a, the cell is an equilateral triangle with a side length l = 14 mm, and the thickness values of the wall and whole structure are b = 1.2 and t = 20 mm, respectively. The cell-enhanced triangular honeycomb is obtained by strengthening the cell on the diagonal of the original triangular honeycomb, as shown in Figure 1b. A small triangle is embedded in the original cell, and the three vertices of the small triangle are located at the midpoint of the three edges of the original cell, respectively, and the wall thickness of the small triangle equals to 1 mm. The wall-enhanced triangular honeycomb is obtained by upgrading the section of the cell wall to an I-beam or I-beam with one side, as shown in Figure 1c. The waist height of the I-beam section of the cell wall is the total thickness of the honeycomb material, which is 20 mm. The waist thickness of the I-beam section is the original thickness of the triangular cell wall, which is 1.2 mm. If the cells on both sides of the cell wall are strengthened, the foot width of the I-beam section of the cell wall is 3.2 mm and the foot thickness is 2 mm. If only one side of the cell wall is strengthened, the section of the cell wall is the I-beam with one side, and the foot width of the I-beam section is 2.2 mm.

The triangular honeycomb structures were all manufactured by the SLM using 316L steel. The SLM is printed along the thickness direction of the whole triangular honeycomb. The thickness of the printing layer is 0.03 mm, the printing speed is 1300 mm/s and the laser power is 370 W.

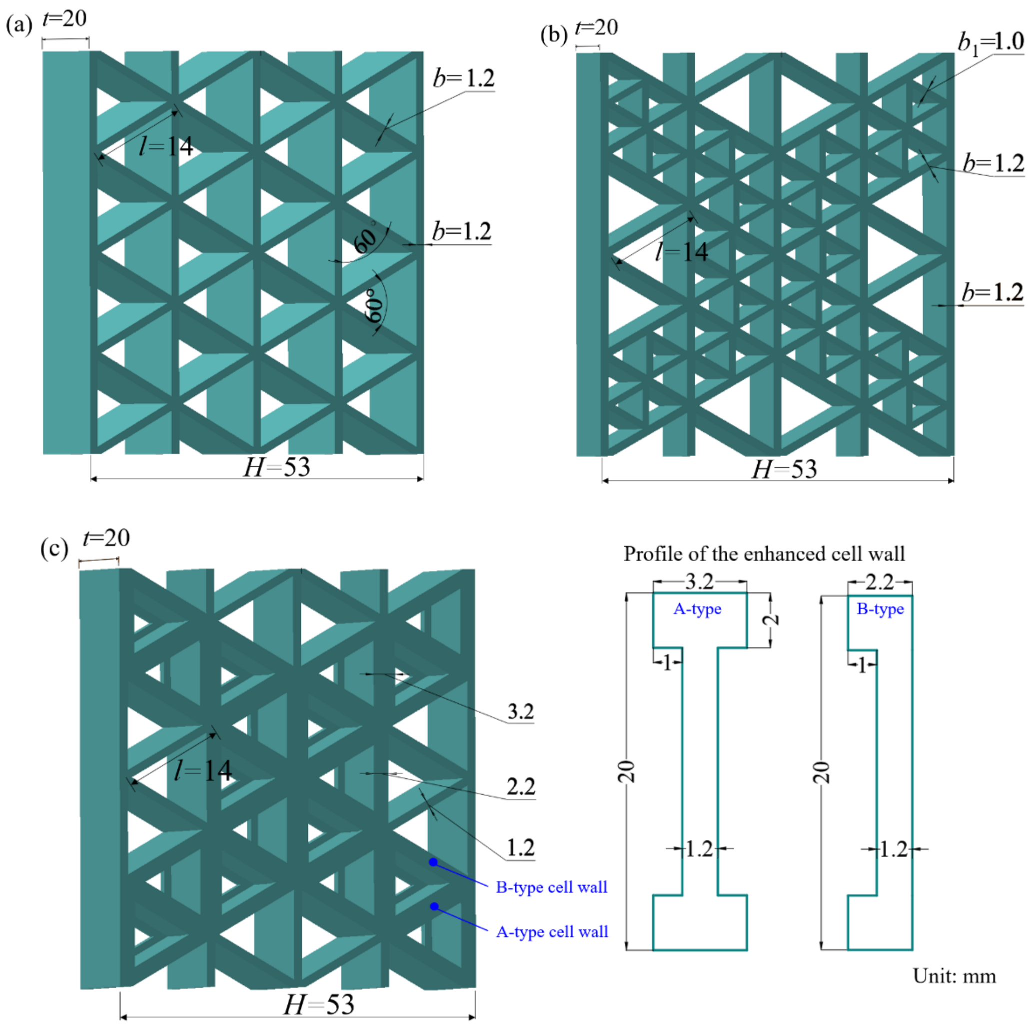

Figure 1. The geometrical configuration of the triangular honeycomb, (**a**) original structure, (**b**) cell-enhanced structure, (**c**) wall-enhanced structure.

Quasi-static compression tests of the original triangular, cell-enhanced triangular and wall-enhanced triangular honeycomb structures were carried out by the universal testing machine with a velocity of 5 mm/min at room temperature. The compression tests were not stopped until the triangular honeycomb samples were compacted.

3. Finite Element Analysis

Finite element analysis (FEA) is performed on the original and locally enhanced triangular honeycomb structures. After element-independent checking, the FEA models of the triangular honeycomb structures are meshed by C3D8R, and the mesh size of $0.8 \times 0.6 \times 0.8$ mm^3 is selected. The final numbers of the element are 51,100, 212,400 and 363,328 for original, cell-enhanced and wall-enhanced triangular honeycomb structures, respectively. The material of the structure was defined as isotropic hardening during the simulation. The upper and lower surfaces of the triangular honeycomb structures each have a plate modelled by discrete rigidity. The displacement compression load is applied to the upper plate with a velocity of 5 mm/min, while the lower plate is completely fixed, as shown in Figure 2. The type of contacting is defined as general contact (coulomb friction contact), and the friction coefficient at the interfaces is set to be 0.3.

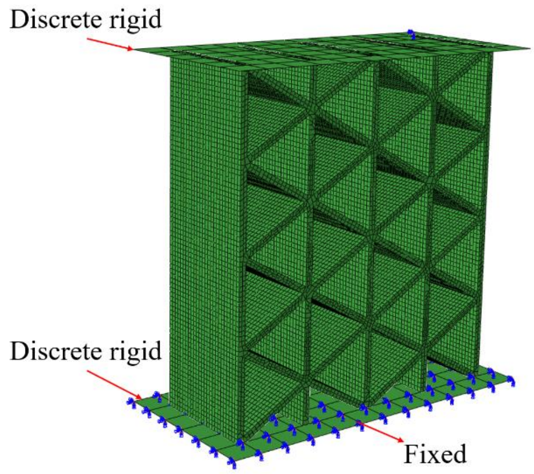

Figure 2. The boundary conditions of the finite element model.

To obtain the properties of the base metal of the triangular honeycomb structures, the uniaxial tensile experiment of 316L steel manufactured by SLM combined with digital image correlation was carried out. The printing direction of the tensile specimen was along the thickness, and the printing parameters were the same as those of the triangular honeycomb structures. The obtained true stress–strain curve of 316L steel manufactured by SLM was shown in Figure 3a. The measured Young's modulus, Poisson's ratio and yield strength are 101.72 GPa, 0.3 and 384.61 MPa, respectively. In order to explore the property difference between traditional manufactured 316L and the SLM 316L, a tensile test of the traditional solid solution 316L steel was also performed, and the true stress–strain curve was shown in Figure 3b. The measured Young's modulus, Poisson's ratio and yield stress of the traditional 316L are 195.16 GPa, 0.3 and 511.27 MPa, respectively.

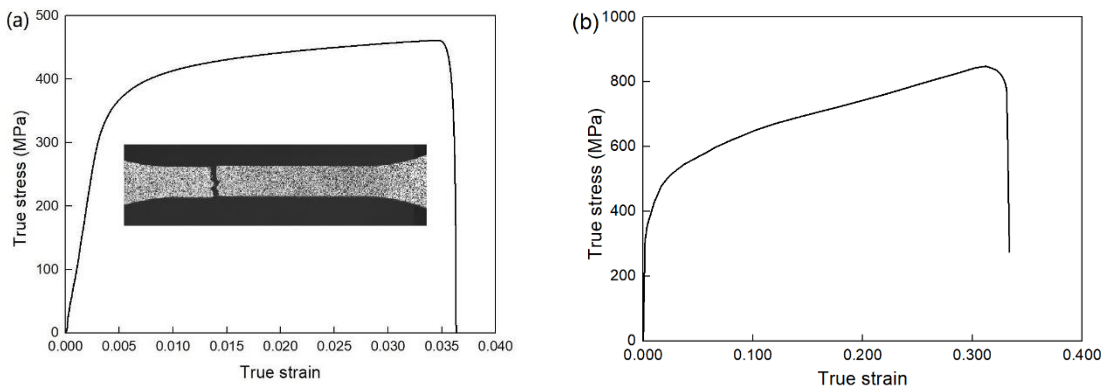

Figure 3. The true stress–strain curve of the 316L steel, (**a**) manufactured by SLM, (**b**) manufactured by traditional method.

Figure 4 shows the fracture morphology of the 316L tensile specimens by scanning electron microscope (SEM). The fracture surface of the tensile specimen is a combination of ductile fracture and brittle fracture, as shown in Figure 4a. The microcosmic appearance in the red circle of Figure 4a is the same as that in Figure 4b, which are smaller dimples. The flat part outside the dimple is a brittle fracture, as shown in Figure 4b. It can also be observed from Figure 4a that there are many unmelted metal particles in the material.

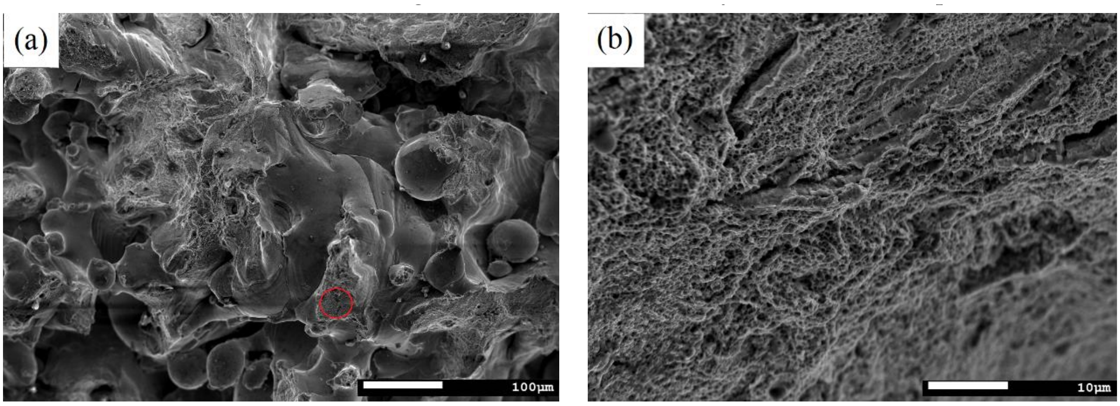

Figure 4. The SEM images of the fracture morphology for tensile specimens, (**a**) the scale of 100 microns, (**b**) the scale of 10 microns.

4. Results and Discussion

4.1. Failure Morphology

The photographs during the deformation and failure process of the triangular honeycomb structures are shown in Figure 5. Figure 5a shows that excessive deformation for the original triangular honeycomb structure occurs at the vertical walls along about 30° to the horizontal direction when macroscopic compressive strain reaches 4%. When the compressive strain increases to 17%, the fracture band has been destroyed seriously, and the excessive deformed unit is completely broken at the node and middle of the wall. With the compression load continuing, a large amount of fracture and failure occur along 30° to the horizontal direction, and almost all the unit cells of the original triangular honeycomb structure are crushed as the compression strain reaches 69%. The individual cell walls of the cell-enhanced honeycomb structure excessively deform at 4% of the compression strain, as shown in Figure 5b. When the compression strain reaches 17%, the upper unit cells of the cell-enhanced structure crack at 30° to the horizontal direction. Subsequently, as the compression strain reaches 38%, a large number of cells are destroyed, except the middle part of the cell-enhanced structure. Figure 5c shows that the deformation of the wall-enhanced honeycomb structure at 4% strain is similar to that of the cell-enhanced honeycomb structure. When the compression strain increases more than 17%, the top half of the wall-enhanced honeycomb structure fails layer by layer. Then, the bottom and middle of the wall-enhanced honeycomb structure are gradually destroyed until the compression strain reaches 63%. Under the action of compression load, the three types of triangular honeycomb structures are all destroyed into fragments.

The simulated compression behaviors of the three triangular honeycomb structures are shown in Figure 6. The deformation behaviors of the three triangular honeycomb structures are all consistent with the experiments. For the original honeycomb structure, the deformation of the vertical walls at the direction of 30° from the horizontal direction leads to stress concentration in the corresponding position for 4% strain. When the strain equals 17%, the stress concentration transfers to the adjacent area after the final failure of the walls. Compared with the original structure, the deformed walls and the high stress area of the cell-enhanced triangular honeycomb structure are somewhat dispersed at 4% strain. The fracture band of the cell-enhanced triangular honeycomb structure is less concentrated than that of the original triangular honeycomb structure for 17% strain. There are few walls excessively deformed for the wall-enhanced triangular honeycomb structures, and the stress distribution is relatively uniform for 4% strain. After the failure of the upper cells, high stress is mainly located at the upper part of the specimen as the strain reaches 17%.

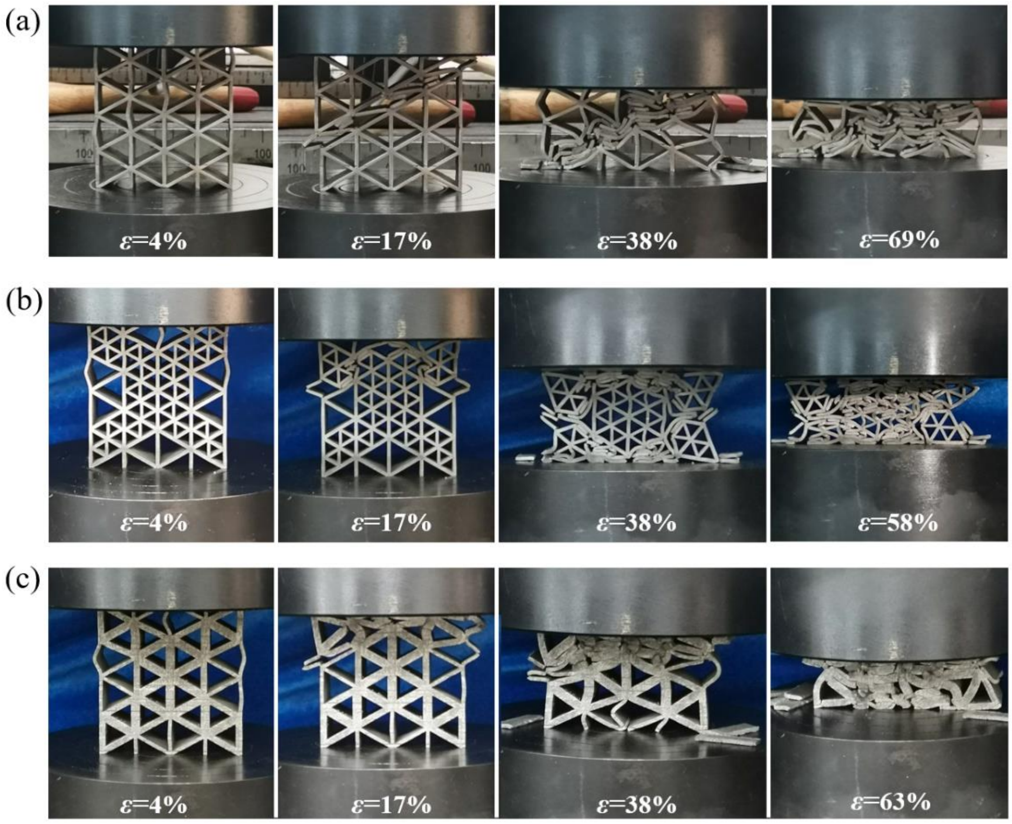

Figure 5. The deformation and failure process of (**a**) original triangular honeycomb structure, (**b**) cell-enhanced triangular honeycomb structure, (**c**) wall-enhanced triangular honeycomb structure.

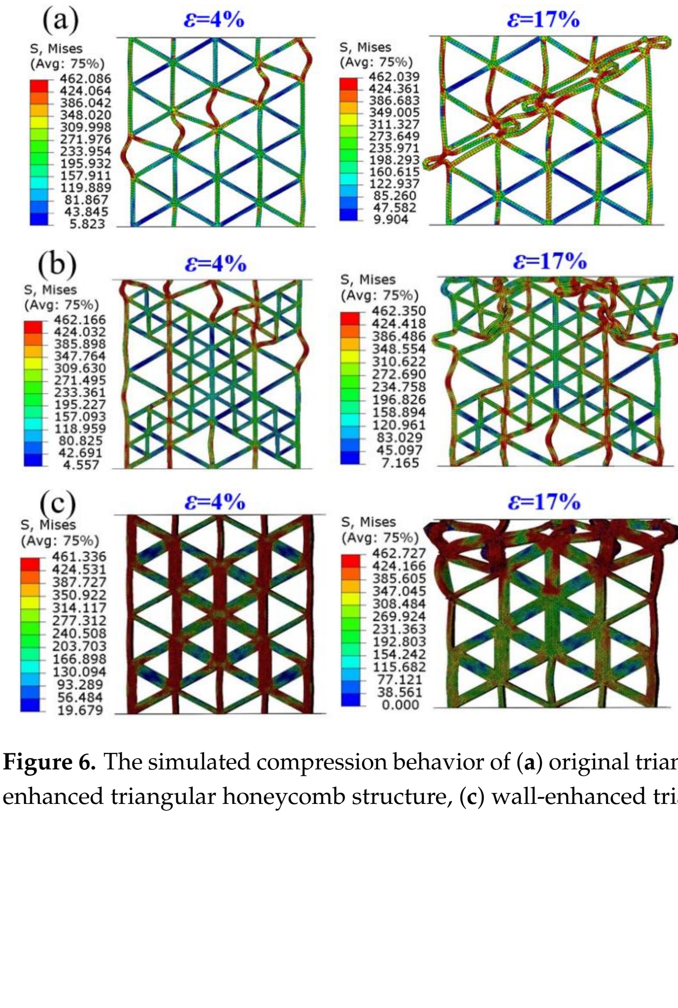

Figure 6. The simulated compression behavior of (**a**) original triangular honeycomb structure, (**b**) cell-enhanced triangular honeycomb structure, (**c**) wall-enhanced triangular honeycomb structure.

4.2. Stiffness and Strength

Figure 7 shows the tested load and displacement curves (F-Δ) of the original, cell-enhanced and wall-enhanced triangular honeycomb structures. The three load–displacement curves are similar, and they all start with a distinct linear elastic stage and then decrease from the first peak load, followed by several peaks and troughs. The occurrence time of the peak load is approximately the same as that of wall buckling. In the end, the curves rise sharply because of the compaction of the honeycomb structure. The compressive load–displacement curve can be divided into three characteristic regions: elastic-plastic region, fracture region and densification region, which can be verified by the results in the literature [36].

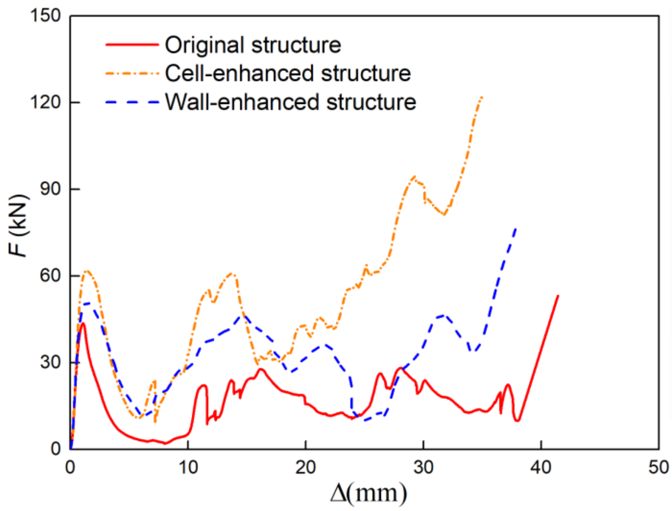

Figure 7. Load (F) and displacement (Δ) curves of the original, cell-enhanced and wall-enhanced triangular honeycomb structures by experiment.

According to the compressive load–displacement curves as shown in Figure 7, the mechanical properties of the three honeycomb structures are listed in Table 1. The stiffness (F/Δ) and peak load of the cell-enhanced structure are the largest, followed by those of the wall-enhanced structure and original structure.

Table 1. The mechanical properties of the original, cell-enhanced and wall-enhanced triangular honeycomb structures obtained by compression tests.

	Stiffness (kN/mm)	**Peak Load (kN)**
Original structure	55.367	43.67
Cell-enhanced structure	65.77	60.78
Wall-enhanced structure	57.56	50.96

4.3. Microstructure Analysis

The block specimens in the scanning plane direction removed from the honeycomb structure are processed by wire cutting technology. After the samples are embedded, the samples are pre-ground on the metallographic grinder with abrasive paper with grades of 180 #, 400 #, 800 #, 1200 # and 1500 #, respectively, and then polished with diamond polishing agents with particle sizes of 9 µm, 6 µm, 3 µm and 0.5 µm, respectively. Figure 8 shows the polished surface of the triangular honeycomb structure by SLM. It is clear that there are many void defects.

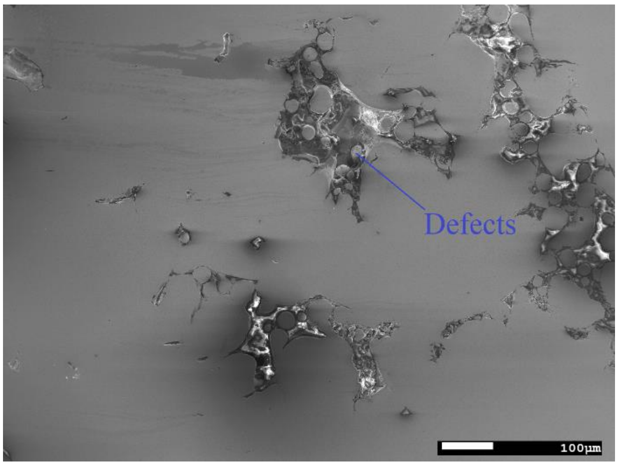

Figure 8. The polished surface in scanning plane direction of triangular honeycomb structure observed by SLM.

Figure 9a,b shows the microstructure of the triangular honeycomb structure in layer by layer forming direction observed by optical microscope. The scale-like fusion lines are clearly visible. The fine grains are distributed in fusion lines, and the size and morphology of the grains in different fusion lines are different. There are obvious epitaxial growth characteristics near the fusion line. During the process of SLM, the laser beam and gas are above the molten pool, and the former solidification layer is below. The molten pool solidifies from the solid substrate to the liquid molten pool due to quick heat transfer. The closer to the former solidification layer, the higher the temperature gradient. The grains always develop towards the fastest direction of heat dissipation so that the columnar crystals formed by SLM begin epitaxial growth along the fusion line [37]. At the same time, local remelting of the former solidified layer occurs near the fusion line, which leads to grain size larger than the center of the molten pool. Figure 9c shows the microstructure of traditional solid solution 316L, which is single-phase austenite, and the grain size is much larger than that of the 316L by SLM.

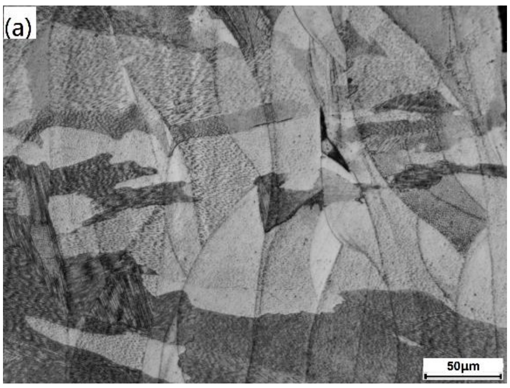

Figure 9. *Cont.*

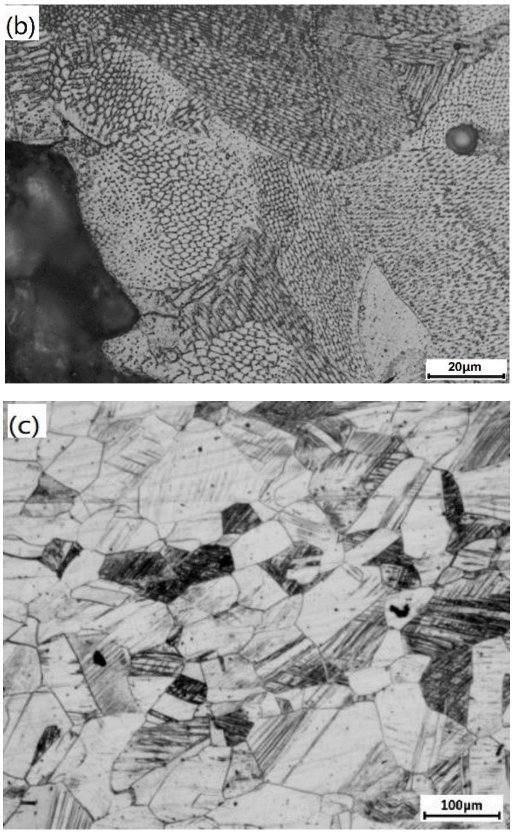

Figure 9. The microstructure of the triangular honeycomb structure in layer by layer forming direction observed by optical microscope, (**a**) fusion lines, (**b**) grain of the 316L by SLM and (**c**) grain of the traditional 316L.

4.4. Discussion

On the basis of the above test results, it can be observed that the failure mode of the original triangular honeycomb structure may be material failure or local buckling. The theoretical method is used to analyze the mechanical properties of the triangular honeycomb structure.

According to the theory of Gibson [38], the equivalent elastic modulus of the original triangular honeycomb structure is

$$\overline{E} = E_{\mathrm{s}}\overline{\rho} \tag{1}$$

where E_{s} is the elastic modulus of the base materials, $\overline{\rho}$ represents the relative density of the honeycomb structure, and it is 27.47% here.

Under the axial compressive load, if the axial stress of any cell wall reaches the yield strength σ_{s}, the honeycomb structure is deemed to have undergone material failure. The equivalent compressive strength of the material failure σ_{m} can be calculated by [27]

$$\sigma_{\mathrm{m}} = \frac{\overline{E}}{E_{\mathrm{s}}}\sigma_{\mathrm{s}} \tag{2}$$

where the symbol σ_{s}, denotes the yield strength of the base material.

Then, the peak load of the material failure can be calculated by

$$P_{\mathrm{m}} = \sigma_{\mathrm{m}} \cdot Ht \tag{3}$$

The local buckling of the honeycomb structure refers to the buckling of the cell wall according to the experimental and simulated results. The possible buckling mode is shown in Figure 10. The deformed vertical wall is regarded as a pole hinged at both ends, and the critical buckling load is

$$P_{\mathrm{cr}} = \frac{\pi^2 E_{\mathrm{s}} I}{l^2} = \frac{\pi^2 E_{\mathrm{s}} H b^3}{12 l^2} \tag{4}$$

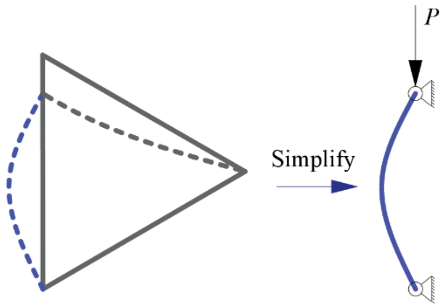

Figure 10. The simplified local buckling model.

For the original honeycomb structure, considering that the horizontal direction of the structure has five buckled cell walls, the peak load of the local buckling mode is

$$P_{\mathrm{b}} = 5 P_{\mathrm{cr}} \tag{5}$$

The calculated compressive strengths of the original honeycomb structure by Equation (3) (material failure) and Equation (5) (local buckling) are 111.99 kN and 73.68 kN, respectively. It is clear that local buckling occurs for the original honeycomb structure first because the calculated peak load by Equation (5) is closer to the experimental value. Based on the above analysis, buckling is the primary factor leading to fracture band for triangular honeycomb structures. Especially for the original honeycomb structure, the ratio of wall thickness to short side is less than 1/10, so the vertical wall at the 30° direction is easy to buckle under the specific topological structure. The strength improvement in the cell-enhanced triangular honeycomb structure and the wall-enhanced triangular honeycomb structure benefits from the reduction in wall buckling. It also indicates that the degree of stress concentration has an important influence on the performance of the triangular honeycomb structures, and the dispersed and lighter stress concentration will improve the performance of the triangular honeycomb structures. In other words, the uniform stress distribution is beneficial to improve the mechanical properties of the structure, which is consistent with the results in the literature [39].

According to Figure 3, both the yield strength and tensile strength of the 316L steel created by SLM in this paper are lower than those of the traditional solid solution 316L steel, which is contrary to the results in the literature [40]. It was mainly caused by the large number of defects, such as unmelted particles and voids, as shown in Figures 4 and 8, and these unusual defects are caused by the manufacturing process in this paper. The elongation at the break of the 316L by SLM is only 11% of that for the traditional solid solution 316L, which means that the plasticity of the 316L by SLM is poor. The unmelted particles and voids reduce the plasticity and strength of the material; therefore, the fracture surface of the tensile specimen is flat, and there is no obvious necking, as shown in Figure 3a. For metals at room temperature, the finer the grains, the higher the strength and the better the plasticity. Although the grain size of the 316L steel created by SLM is small, as shown in Figure 9b, the manufactured defects have a great negative effect so that the strength and plasticity of the SLM 316L steel are lower than those of the traditional solid solution 316L.

Although the base metal manufactured by SLM in this paper is very brittle, for the original triangular honeycomb structure under the in-plane compression load, the appearance of the fracture band cannot be explained using the method that the shear stress in the direction of 45° to the load is the maximum. As the triangular honeycomb structure first undergoes local buckling, the brittleness of the base metal causes the honeycomb structure to disperse into fragments with continuous compression loading. To make the stress distribution of the structure more uniform is a general method to avoid fracture band and improve the strength of the honeycomb structure.

5. Conclusions

In this paper, two locally enhanced triangular honeycomb structures, namely cell-enhanced and wall-enhanced triangular honeycomb structures, were proposed to avoid diagonal fracture band failure. The in-plane compressive behaviors of the original and locally enhanced triangular honeycomb structures manufactured by SLM were investigated by the experiment and simulation. The failure mechanism of the triangular honeycomb structures was analyzed in detail. Based on this study, the following conclusions have been drawn:

(1) The cell-enhanced and wall-enhanced honeycomb structures possess higher stiffness and peak load than the original honeycomb structure, in which the peak load of the cell-enhanced structure is the largest. The peak load of the triangular honeycomb structure is related to the stress concentration. Uniform stress distribution is beneficial to improve the mechanical properties of the structure.
(2) The locally enhanced method can effectively optimize the diagonal fracture band failure of triangular honeycomb materials. The fracture band of the cell-enhanced triangular honeycomb structure under compressive load becomes more localized, while the wall-enhanced structure fails layer by layer.
(3) For the triangular honeycomb structure under in-plane compression, the appearance of the fracture band is caused by the buckling of the walls, which is related to the topological structure.
(4) The grain of SLM 316L steel is very fine, and the grain morphology in different scales is different. The unmelted particles and voids reduce the plasticity and strength of the SLM 316L steel greatly.

Author Contributions: Conceptualization, Q.Z. and W.W.; methodology Q.Z.; software, Q.Z.; validation, Q.Z.; investigation, Q.Z. and J.L.; resources, W.W.; writing—original draft preparation, Q.Z.; writing—review and editing, W.W. and J.L. All authors have read and agreed to the published version of the manuscript.

Funding: This research was funded by the Natural Science Foundation of Shandong Province (Grants No.: ZR2021QE099), the National Natural Science Foundation of China (Grants No.: 52205175), the Key R&D Program of Shandong Province (Grants No.: 2021CXGC011302), China Postdoctoral Science Foundation (Grants No.: 2020M682257) and Fundamental Research Funds for the Central Universities (Grants No.: 20CX06099A).

Institutional Review Board Statement: Not applicable.

Informed Consent Statement: Not applicable.

Data Availability Statement: The data presented in this study are available in this article.

Conflicts of Interest: The authors declare no conflict of interest.

References

1. DebRoy, T.; Mukherjee, T.; Milewski, J.O.; Elmer, J.W.; Ribic, B.; Blecher, J.J.; Zhang, W. Scientific, technological and economic issues in metal printing and their solutions. *Nat. Mater.* **2019**, *18*, 1026–1032. [CrossRef] [PubMed]
2. Sabban, R.; Bahl, S.; Chatterjee, K.; Suwas, S. Globularization using heat treatment in additively manufactured Ti-6Al-4V for high strength and toughness. *Acta Mater.* **2019**, *162*, 239–254. [CrossRef]
3. Ge, J.; Lin, J.; Lei, Y.; Fu, H. Location-related thermal history, microstructure, and mechanical properties of arc additively manufactured 2Cr13 steel using cold metal transfer welding. *Mater. Sci. Eng. A* **2018**, *715*, 144–153. [CrossRef]
4. Liu, S.Y.; Shin, Y.C. Additive manufacturing of Ti6Al4V alloy: A review. *Mater. Des.* **2019**, *164*, 107552. [CrossRef]
5. Ngo, T.D.; Kashani, A.; Imbalzano, G.; Nguyen, K.T.Q.; Hui, D. Additive manufacturing (3D printing): A review of materials, methods, applications and challenges. *Compos. Part B Eng.* **2018**, *143*, 172–196. [CrossRef]

6. DebRoy, T.; Wei, H.L.; Zuback, J.S.; Mukherjee, T.; Elmer, J.W.; Milewski, J.O.; Beese, A.M.; Wilson-Heid, A.; De, A.; Zhang, W. Additive manufacturing of metallic components–Process, structure and properties. *Prog. Mater. Sci.* **2018**, *92*, 112–224. [CrossRef]
7. Nazir, A.; Abate, K.M.; Kumar, A.; Jeng, J.Y. A state-of-the-art review on types, design, optimization, and additive manufacturing of cellular structures. *Int. J. Adv. Manuf. Technol.* **2019**, *104*, 3489–3510. [CrossRef]
8. Wang, P.; Zheng, Z.; Liao, S.; Yu, J. Strain-rate effect on initial crush stress of irregular honeycomb under dynamic loading and its deformation mechanism. *Acta Mech. Sinica-Prc.* **2017**, *34*, 117–129. [CrossRef]
9. Ashab, A.S.M.; Ruan, D.; Lu, G.; Wong, Y.C. Quasi-static and dynamic experiments of aluminum honeycombs under combined compression-shear loading. *Mater. Des.* **2016**, *97*, 183–194. [CrossRef]
10. Zhao, Y.; Ge, M.; Ma, W. The effective in-plane elastic properties of hexagonal honeycombs with consideration for geometric nonlinearity. *Compos. Struct.* **2020**, *234*, 111749.
11. Liang, S.; Chen, H.L. Investigation on the square cell honeycomb structures under axial loading. *Compos. Struct.* **2006**, *72*, 446–454. [CrossRef]
12. Langrand, B.; Casadei, F.; Marcadon, V.; Portemont, G.; Kruch, S. Experimental and finite element analysis of cellular materials under large compaction levels. *Int. J. Solids Struct.* **2017**, *128*, 99–116. [CrossRef]
13. Zhang, X.; Zhang, H. Theoretical and numerical investigation on the crush resistance of rhombic and kagome honeycombs. *Compos. Struct.* **2013**, *96*, 143–152. [CrossRef]
14. Hohe, J.; Becker, W. Effective elastic properties of triangular grid structures. *Compos. Struct.* **1999**, *45*, 131–145. [CrossRef]
15. Liu, W.; Li, H.; Zhang, J.; Bai, Y. In-plane mechanics of a novel cellular structure for multiple morphing applications. *Compos. Struct.* **2019**, *207*, 598–611. [CrossRef]
16. Zhang, D.; Fei, Q.; Zhang, P. In–plane dynamic crushing behavior and energy absorption of honeycombs with a novel type of multi-cells. *Thin-Walled Struct.* **2017**, *117*, 199–210. [CrossRef]
17. Yang, X.; Xi, X.; Pan, Q.; Liu, H. In-plane dynamic crushing of a novel circular-celled honeycomb nested with petal-shaped mesostructure. *Compos. Struct.* **2019**, *226*, 111219. [CrossRef]
18. Peng, X.L.; Bargmann, S. A novel hybrid-honeycomb structure: Enhanced stiffness, tunable auxeticity and negative thermal expansion. *Int. J. Mech. Sci.* **2021**, *190*, 106021. [CrossRef]
19. Deshpande, A.S.; Burgert, I.; Paris, O. Hierarchically structured ceramics by highprecision nanoparticle casting of wood. *Small* **2006**, *2*, 994–998. [CrossRef]
20. Weaver, J.C.; Aizenberg, J.; Fantner, G.E.; Kisailus, D.; Woesz, A.; Allen, P.; Fields, K.; Porter, M.J.; Zok, F.W.; Hansma, P.K.; et al. Hierarchical assembly of the siliceous skeletal lattice of the hexactinellid sponge Euplectella aspergillum. *J. Stuct. Biol.* **2007**, *158*, 93–106. [CrossRef]
21. Nassiraei, H.; Rezadoost, P. Stress concentration factors in tubular T/Y-joints strengthened with FRP subjected to compressive load in offshore structures. *Int. J. Fatigue* **2020**, *140*, 105719. [CrossRef]
22. Nassiraei, H.; Rezadoost, P. Static capacity of tubular X-joints reinforced with fiber reinforced polymer subjected to compressive load. *Eng. Struct.* **2021**, *236*, 112041. [CrossRef]
23. Fang, J.; Sun, G.; Qiu, N.; Pang, T.; Li, S.; Li, Q. On hierarchical honeycombs under out-of-plane crushing. *Int. J. Solids Struct.* **2018**, *135*, 1–13. [CrossRef]
24. Chen, Y.; Li, T.; Jia, Z.; Scarpa, F.; Yao, C.W.; Wang, L. 3D printed hierarchical honeycombs with shape integrity under large compressive deformations. *Mater. Des.* **2018**, *137*, 226–234. [CrossRef]
25. Nassiraei, H. Static strength of tubular T/Y-joints reinforced with collar plates at fire induced elevated temperature. *Mar. Struct.* **2019**, *67*, 102635. [CrossRef]
26. Nassiraei, H.; Zhu, L.; Lotfollahi-Yaghin, M.A.; Ahmadi, H. Static capacity of tubular X-joints reinforced with collar plate subjected to brace compression. *Thin Wall Struct.* **2017**, *119*, 256–265. [CrossRef]
27. Li, M.; Lai, C.L.; Zheng, Q.; Han, B.; Wu, H.; Fan, H.L. Design and mechanical properties of hierarchical isogrid structures validated by 3D printing technique. *Mater. Des.* **2019**, *168*, 107664. [CrossRef]
28. Fan, H.; Luo, Y.; Yang, F.; Li, W. Approaching perfect energy absorption throughstructural hierarchy. *Int. J. Eng. Sci.* **2018**, *130*, 12–32. [CrossRef]
29. Oftadeh, R.; Haghpanah, B.; Papadopoulos, J.; Hamouda, A.M.S.; Nayeb-Hashemi, H.; Vaziri, A. Mechanics of anisotropic hierarchical honeycombs. *Int. J. Mech. Sci.* **2014**, *81*, 126–136. [CrossRef]
30. He, Q.; Feng, J.; Zhou, H. A numerical study on the in-plane dynamic crushing of selfsimilar hierarchical honeycombs. *Mech. Mater.* **2019**, *138*, 103151. [CrossRef]
31. Zhang, D.; Fei, Q.; Jiang, D.; Li, Y. Numerical and analytical investigation on crushing of fractal-like honeycombs with self-similar hierarchy. *Compos. Struct.* **2018**, *192*, 289–299. [CrossRef]
32. Liu, L.; Kamm, P.; García-Moreno, F.; Banhart, J.; Pasini, D. Elastic and failure response of imperfect three-dimensional metallic lattices: The role of geometric defects induced by selective laser melting. *J. Mech. Phys. Solids* **2017**, *107*, 160–184. [CrossRef]
33. Du Plessis, A.; Razavi, S.M.J.; Berto, F. The effects of microporosity in struts of gyroid lattice structures produced by laser powder bed fusion. *Mater. Des.* **2020**, *194*, 108899. [CrossRef]
34. Roach, A.M.; White, B.C.; Garland, A.; Jared, B.H.; Carroll, J.D.; Boyce, B.L. Size-dependent stochastic tensile properties in additively manufactured 316L stainless steel. *Addit. Manuf.* **2020**, *32*, 101090. [CrossRef]

35. Gu, H.Y.; Pavier, M.; Shterenlikht, A. Experimental study of modulus, strength and toughness of 2D triangular lattices. *Int. J Solids Struct.* **2018**, *152–153*, 207–216. [CrossRef]
36. Ge, J.G.; Yan, X.C.; Lei, Y.P.; Ahmed, M.; O'Reilly, P.; Zhang, C.; Lupoi, R.; Yin, S. A detailed analysis on the microstructure and compressive properties of selective laser melted Ti6Al4V lattice structures. *Mater. Des.* **2021**, *198*, 109292. [CrossRef]
37. Zhong, Y.; Liu, L.F.; Wikman, S.; Cui, D.Q.; Shen, Z.J. Intragranular cellular segregation network structure strengthening 316L stainless steel prepared by selective laser melting. *J. Nucl. Mater.* **2016**, *470*, 170–178. [CrossRef]
38. Gibson, L.J.; Ashby, M.F. *Cellular Solids: Structure and Properties*; Cambridge University Press: Cambridge, UK, 1999; pp. 655–656.
39. Liu, Y.J.; Ren, D.C.; Li, S.J.; Wang, H.; Zhang, L.C.; Sercombe, T.B. Enhanced fatigue characteristics of a topology-optimized porous titanium structure produced by selective laser melting. *Addit. Manuf.* **2020**, *32*, 101060. [CrossRef]
40. Tolosa, I.; Garciandia, F.; Zubiri, F.; Zapirain, F.; Esnaola, A. Study of mechanical properties of AISI 316stainless steel processed by "selective laser melting", following different manufacturing strategies. *Int. J. Adv. Manuf. Tech.* **2010**, *51*, 639–647. [CrossRef]